Supporting information

A Multi-layer Flexible Photothermal TiN based Superhydrophobic Surface for highly efficient Anti-Icing and De-Icing

Ji Bowen,‡[a] Chen Tianchi,‡*[a] Song Xuqing,[a] Sheng Lianchao,[a] Lu Xiangning,[a]and Yang Daolong[a]

School of Mechanical and Electrical Engineering, Jiangsu Normal University, Xuzhou 221000, China.

*corresponding author：ctc900112@163.com

Total number of pages: 24

Total number of figures: 27

Total number of tables: 2

Content

1. Testing details

1.1 Mechanical durability and chemical stability tests

The mechanical robustness of the composite superhydrophobic coating was evaluated by sandpaper abrasion tests and sand impact cycling test. For the sandpaper abrasion tests, the sample was placed horizontally on the table with the 400# sandpaper in contact with the sample. A 100 g weight (~ 2.2 kPa) is placed on the sample and a horizontal force is applied. It moves at a speed of 5 cm/s. A total of 50 cycles were carried out, and the sliding distance of each cycle was 20cm. After 50 cycles, CA and SA were measured respectively. For the sand impact cycling test, 200 g sand particles with diameters ranging from 100 to 200 mesh were released freely from a sand container placed ~30 cm above the sample which was tilted by 40° in each impact cycle . The WCA and SA were measured after five abrasion cycles. The environmental robustness of multi-layer superhydrophobic coatings was evaluated by testing the ability of superhydrophobic coatings to maintain superhydrophobicity at ambient temperatures of -40℃ and 200℃, and the CA and SA at ambient temperature were measured every 2h.

Chemical stability was assessed by chemical solution soaking test and measurements of wetting behavior in several chemical solutions. Firstly, WCA and SA of ML-SHs was measured by aqueous solutions with different pH values ranging from 1 to 14. The as-prepared multi-layered flexible photothermal superhydrophobic samples were immersed in water, acid solution (pH = 1, hydrochloric acid adjustment) and alkali solution (pH = 10, sodium hydroxide adjustment), and ethanol. After the test time of 24h, the samples were washed and dried. Then contact and sliding angles were measured subsequently.

1.2 Passive anti-icing, active deicing and ice adhesion experiments

The passive anti-icing and active deicing performance of the coatings were investigated in a environmental test chamber (TL-100, Expery Environmental Test Equipment Co., LTD, China). To evaluate the passive anti-icing performance of the coatings, the freezing process and the icing delay time of the droplets (20 μl) on the uncoated substrates, SHs and ML-SHs coatings in the -5 °C - -40 °C, relative humidity = 35 ± 5% environment were recorded with a camera. The icing delay time was defined as the time for a droplet to change from liquid phase to solid phase until it was completely transformed into ice during the freezing process. T_{in} (icing nucleation time) is defined as the time it takes the droplet to contact the surface from transparent to opaque, and T_{if} (icing freezing time) is the transition from the beginning of the phase transition to a fully frozen droplet.

In order to evaluate the active deicing performance of the coatings, a camera was used to

record the time when the ice melted completely away from the coating surface under the simulated solar radiation (0.5sun, 0.75sun and 1sun) of the xenon light source under the environment of -10℃ to -30℃. Specifically, the water was frozen on the coating to form an ice layer of a thickness of approximately 2 mm in a cold environment (-20℃). Then the sample was placed in a freezer at a temperature of -10 °C - -30 °C, relative humidity of 35 ± 5% for another 1h and then irradiated with a xenon lamp under simulated sunlight with a light intensity of 0.5sun, 0.75sun and 1sun. The active deicing process and the deicing time were recorded with a camera.

The samples were placed in a environmental test chamber (GDW-0150, Wuxi Nanya Sci-Tech Co., Ltd, China) with the temperature and humidity set to -20°C and 35 ± 5% RH, respectively. A acrylic column with a base area of 100 mm^2 and a height of 5cm was placed on the samples, deionized water was injected into the column, and the deionized water was completely frozen after 1 hours. After the samples were completely fixed, the force transducer was mounted on the motion stage to push the column at a rate of 0.2mm/s. The maximum force was recorded to calculate the ice adhesion strength by the equation:

$$\tau_{ice} = \frac{F_{max}}{A} \quad \text{(S1)}$$

where A stands for the contact area between the ice and surface. ice adhesion strength were average values for 3 times.

2. Calculation and Modeling details

S1. Calculating the light absorption efficiency

Light absorbance of the samples is calculated through the following equation:

$$A\% = 1 - R\% - T\% \quad \text{(S3)}$$

where A is the absorbance, R is the reflectance, and T is the transmittance.

S2. Calculating the photothermal conversion efficiency

The photothermal conversion efficiency of samples, η, which was defined as the ratio of the heat generated by the photothermal conversion of the surface to the input of solar power, and the calculation formula is as follows:

$$\eta = \frac{Q}{q \times A} \quad \text{(S4)}$$

where Q is the total heat generated by the surface, q represents the light intensity of sunlight (1kW/m^2), A is the surface area of the surface (6.25 cm^2).

When the surface temperature of samples and the surrounding temperature gradually reach a balance, the heat generated by the surface can be calculated as follows:

$$Q = h \times A \times (T_{sub} - T_{surr}) \quad \text{(S5)}$$

where h is the convective heat transfer coefficient of the substrate, A is the heat transfer area, T_{sub} is the equilibrium temperature of the surface, and T_{surr} is the temperature of surrounding temperature.

The convective heat transfer coefficient of the samples can be calculated by the following equation:

$$h = \frac{N\mathrm{u} \times \lambda}{L} \quad \text{(S6)}$$

where L is the characteristic length of heat transfer area (L=2.5), λ is the thermal conductivity of air, N_u is the Nusselt number, and can be calculated as follows:

$$N\mathrm{u} = 0.54 \times (Gr \times \mathrm{Pr})_m^{1/4} \quad \text{(S7)}$$

where $Gr = \frac{g a_v \Delta T L^3}{v^2}$ is the Grashof number, Pr is the prandtl number, the m represents qualitative temperature, which use arithmetic average temperature of the boundary layer ($T_m = \frac{T_{sub} + T_{surr}}{2}$). a_v is the expansion coefficient of air ($a_v = \frac{1}{T}$), T is the average of the sum of the initial ambient and equilibrium temperatures of the sample, g is the gravitational acceleration (9.8 m/s^2). ΔT is the value of the temperature difference in surface from room temperature to equilibrium temperature, ν is the viscosity coefficient.

S3. The heat-transfer model of a droplet on the uncoated hydrophilic surfaces, hydrophobic surface with Wenzel model and ML-SHs with Cassie model under cold conditions.

The finite element simulation methods were performed by COMSOL, and the detailed method was explained as follows:

(1) The initial ambient temperature was -20 °C, the initial temperature of water droplet was 0 °C. We neglected the evaporation of water and sublimation of ice in the cooling conditions.

(2) The CA of the water droplet on the hydrophilic surface was 30°, the CA of the water droplet on the hydrophobic surface was 130°, the CA of the water droplet on the superhydrophobic surface was 150°.

(3) The classical heat and mass transfer equations were still feasible.

$$\frac{\partial(\rho C_p T)}{\partial t} + \nabla(\rho C_p u T) = \nabla[\nabla(kT)] \tag{S8}$$

(4) The networks near the heat transfer interfaces was set to hyperfine structure. The minimum interval step of time simulation was 0.001s.

Note S4. Calculating temperature distribution in photothermal process

A COMSOL model were built to analyze the temperature distribution of the SHs and ML-SHs under the transient analysis mode. The thermal energy input of the computed model can be calculated in the Eq.(S1). The heat transfer model in the different evaporators could be calculated by the equation given as following:

$$\rho C_P \frac{\partial T}{\partial t} + \rho C C_P u \cdot \nabla T + \nabla \cdot q = Q \tag{S9}$$

$$q = -k\nabla T \tag{S10}$$

, where T is the temperature, u is the fluid flow speed; ρ is the density, C_p is the special heat capacity and k is the thermal conductivity. In the mode simulation, the initial ambient temperature was -15 °C, the final condition of transient analysis was set to t = 1800s.

Note S5. The fluid dynamics model of a droplet on the untreated and ML-SHs surfaces.

The finite element simulation was performed by COMSOL to analysis the fluid dynamics of the water droplet. The multiphase flow model was level-set methods . Before simulation, the following conditions were set:

(1)The initial ambient temperature was 0 ºC, the initial temperature of water droplet was also 0 ºC. The evaporation and sublimation of water were neglected.

(2) The wettability wall was set to 150° on the superhydrophobic surface. The wettability wall was set to 30° on the hydrophilic surface. The volume of water droplet on different surfaces is the same. The movement of air and water was set to laminar flow model.

(3) The movement of air and water can be described by the Navier-Stokes equations. The solid substrate was fixed with an inclination of 30°. The networks of the whole model was set to hyperfine structure. The minimum interval step of time simulation was 0.001s.

3.Supplementary Figures

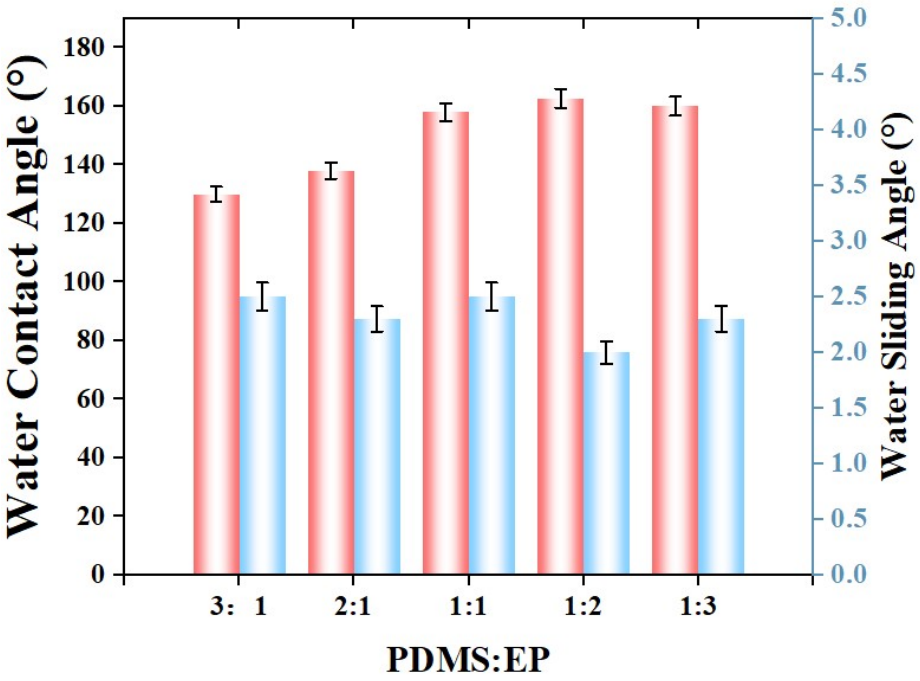

Fig. S1 Water contact angle and sliding angle of the ML-SHs coatings with different ratio of EP and PDMS.

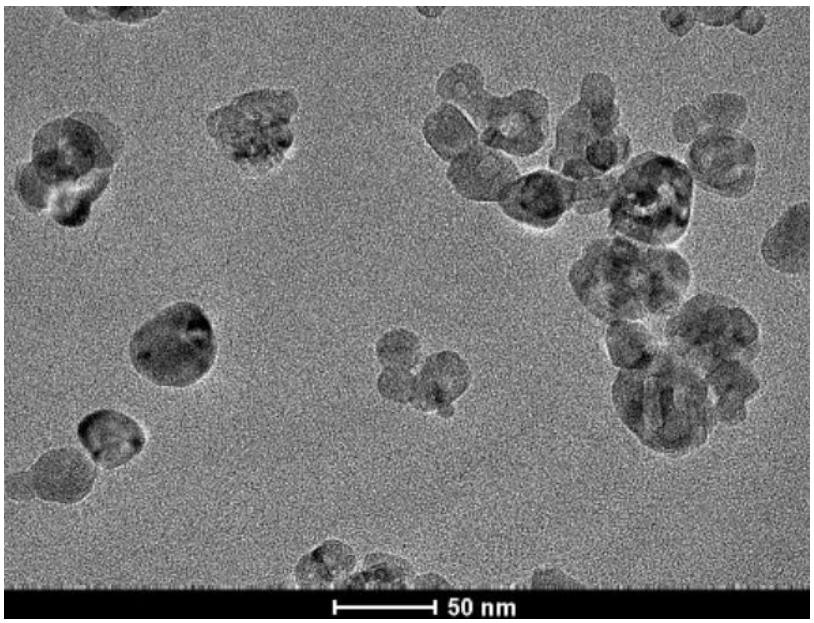

Fig. S2 TEM images of TiN nanoparticles

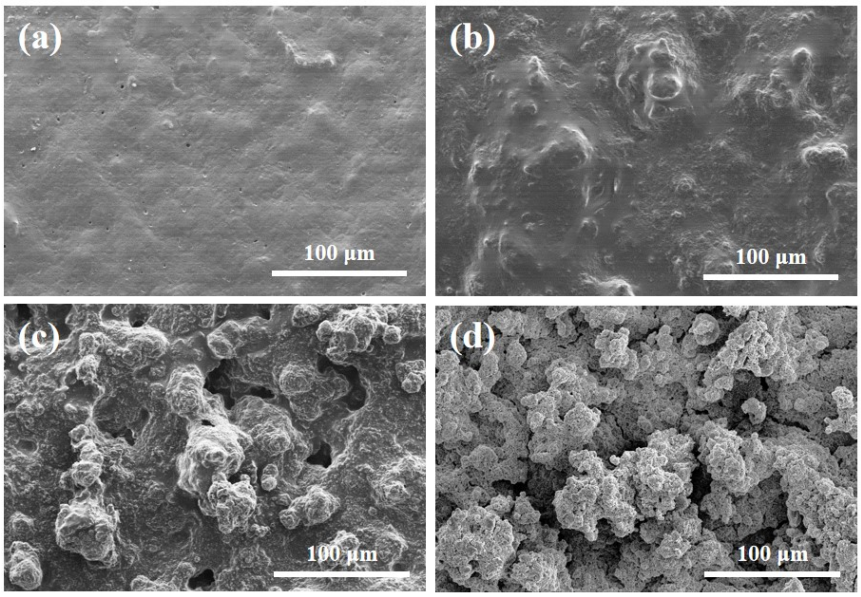

Fig. S3 SEM images of samples with different mass of SiO_2 particles (a) 0g, (b) 0.25g, (c) 0.5g and (d) 0.75g.

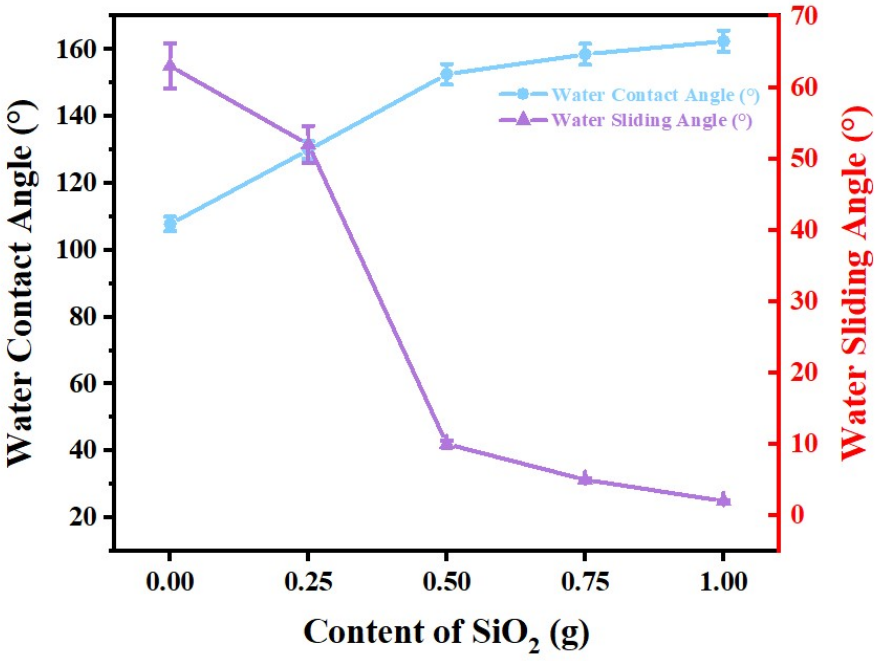

Fig. S4 Water contact angle and sliding angle of the ML-SHs coatings with different mass of SiO_2

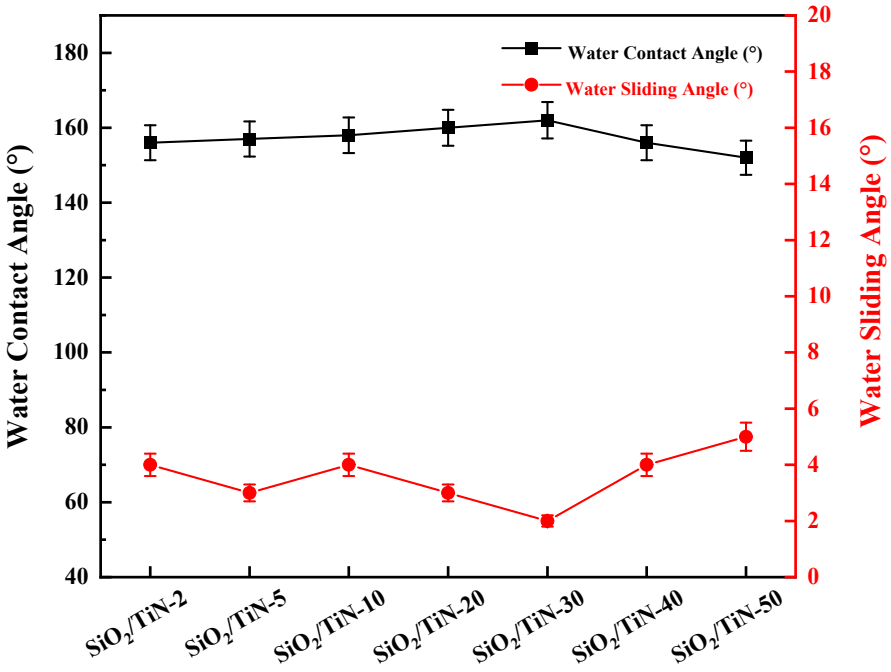

Fig. S5 Water contact angle and sliding angle of the ML-SHs coatings with different mass percentages of TiN

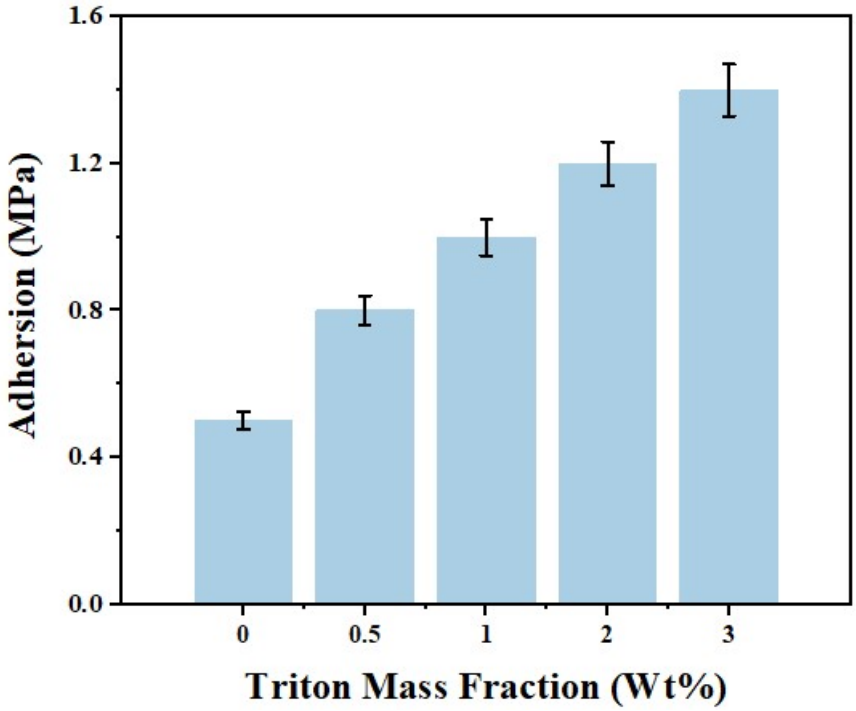

Fig. S6 Adhesion under layers of Triton X-100 with different additive levels

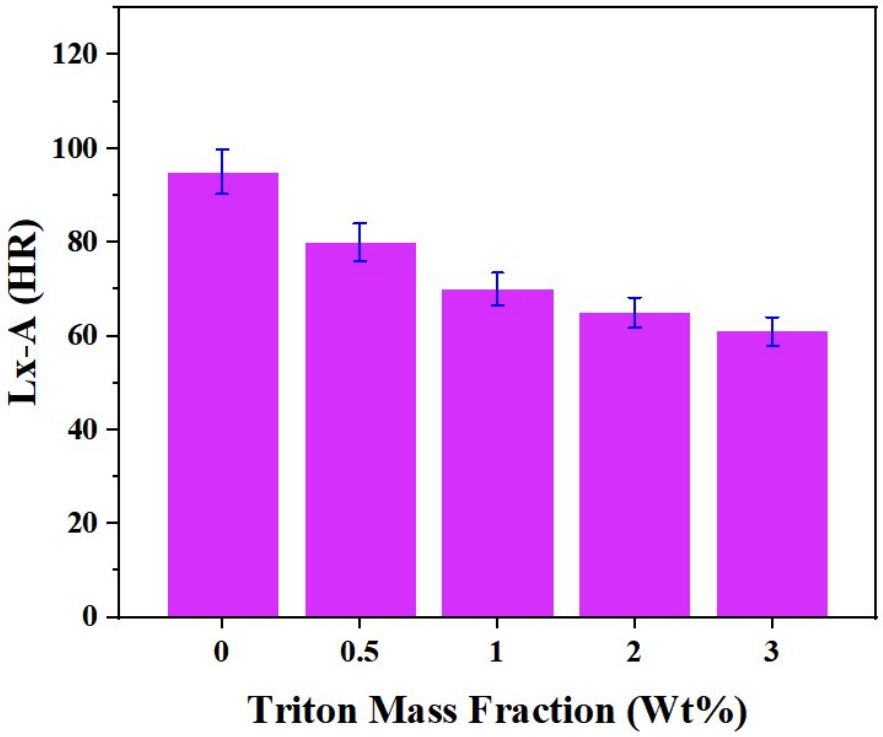

Fig. S7 Shore hardness values under layers of Triton X-100 with different levels of additives

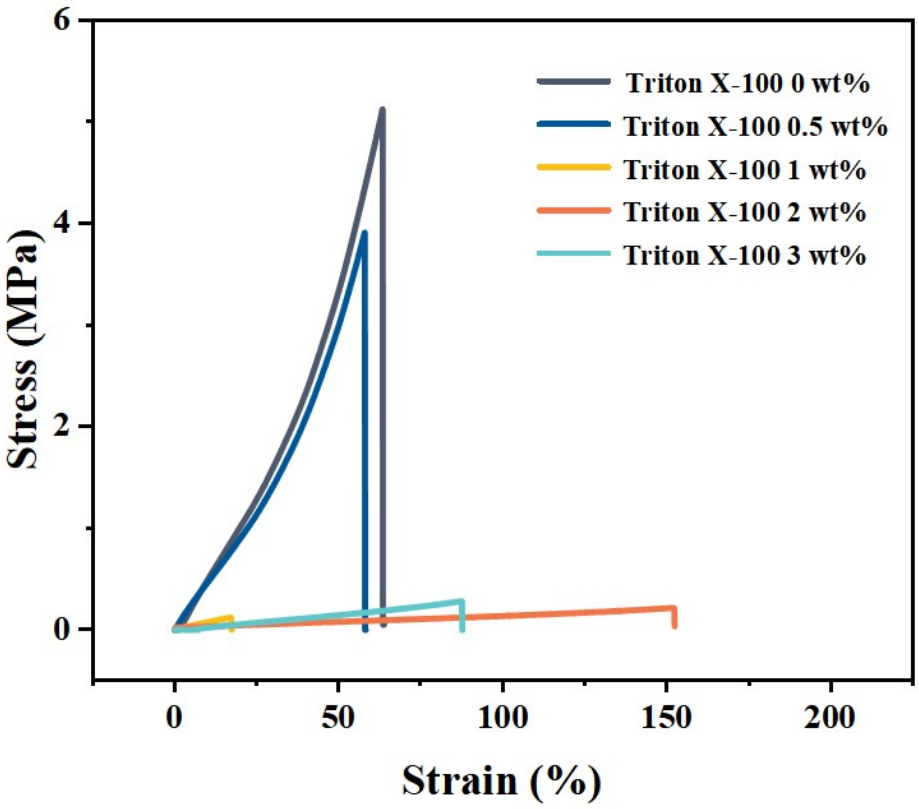

Fig. S8 Stress-strain diagrams under different levels of Triton X-100 layers

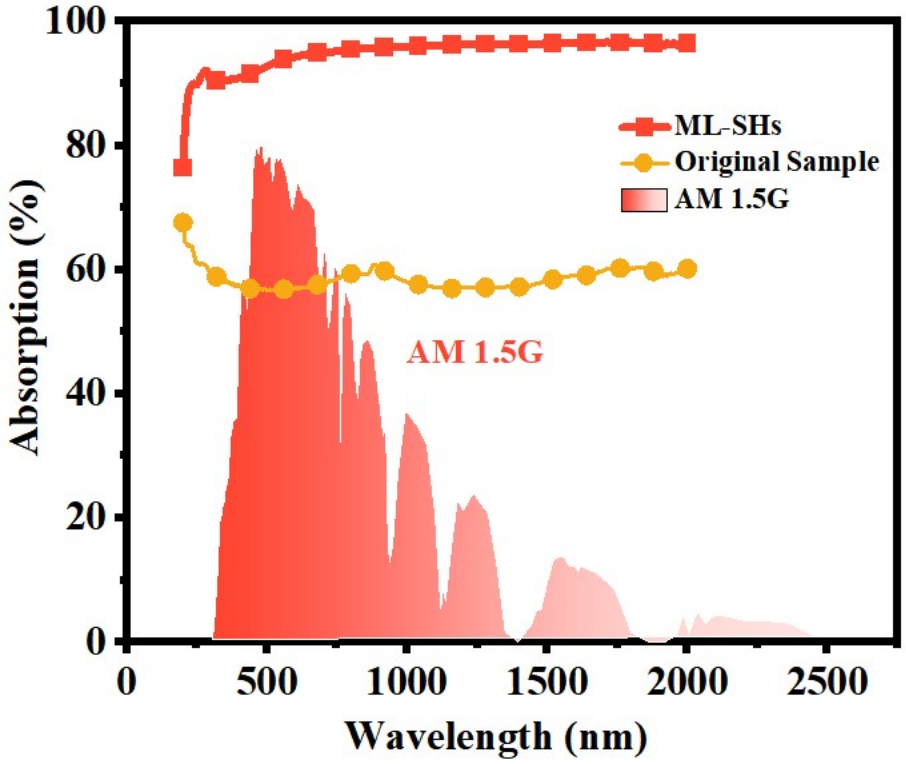

Fig. S9 The light absorption spectrum in the 250-2000 nm wavelength range of the uncoated sample and ML-SHs

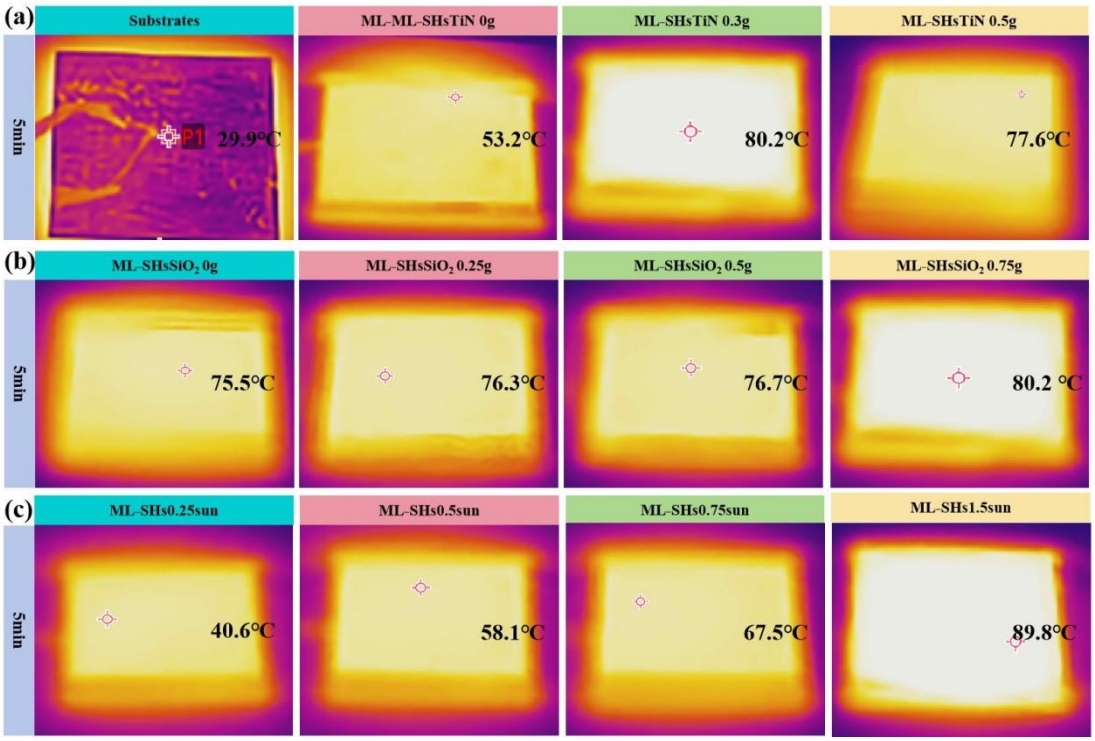

Fig. S10 Equilibrium temperature thermal infrared photographs of an uncoated substrate and ML-SHs with different mass of TiN and SiO_2 under different solar irradiation densities, (a) TiN contents, (b) SiO_2 contents, and (c) solar irradiation densities

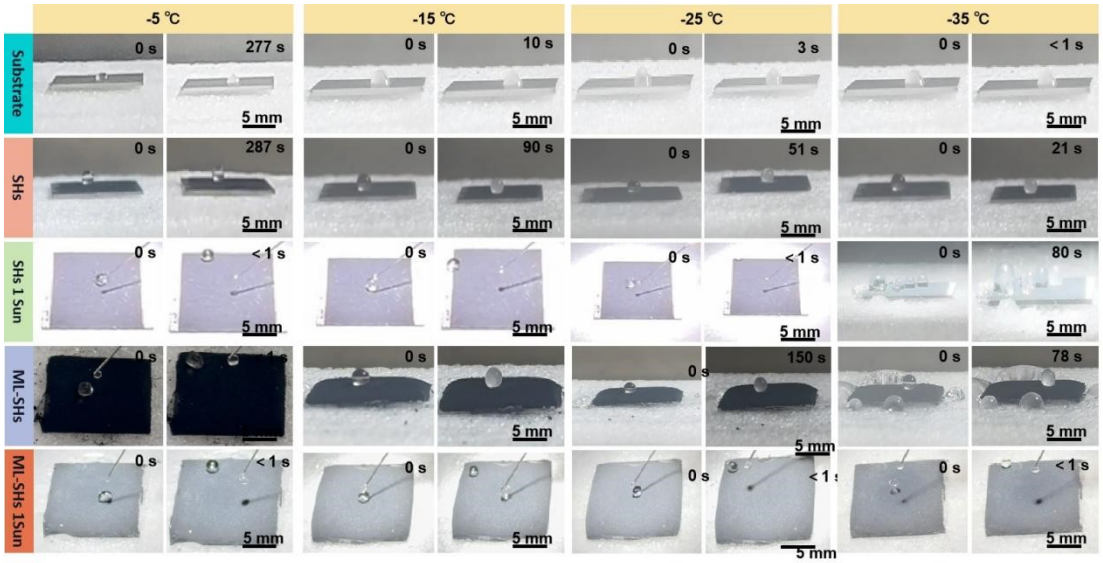

Fig. S11 Icing delay process on the untreated surface, the SHs surface, and the ML-SHs surface at temperatures ranging from -5°C to -35°C.

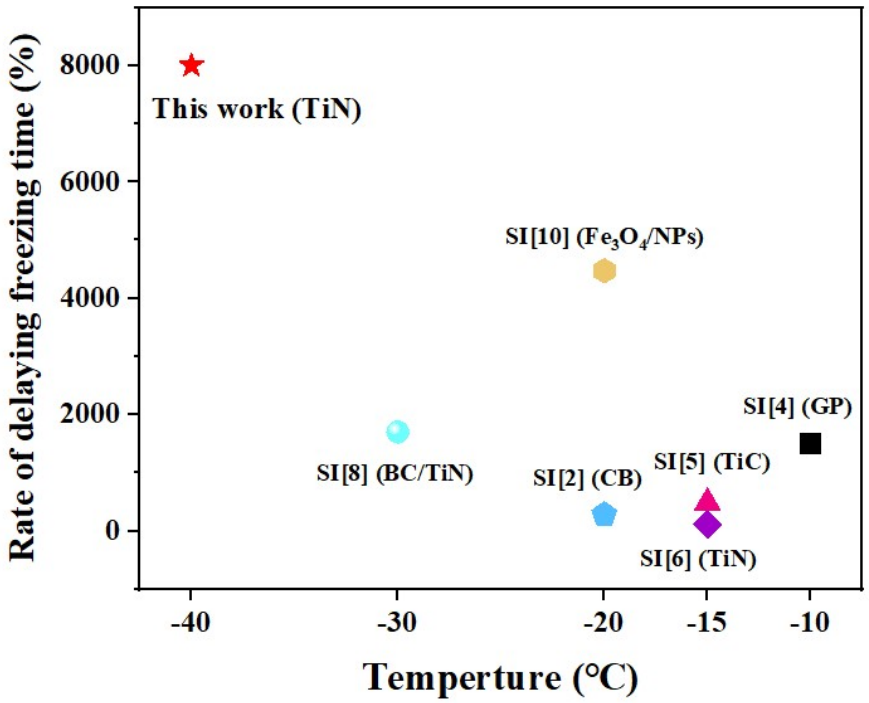

Fig.S12 The comparison of rate of delayed freezing time of ML-SHs with other literatures

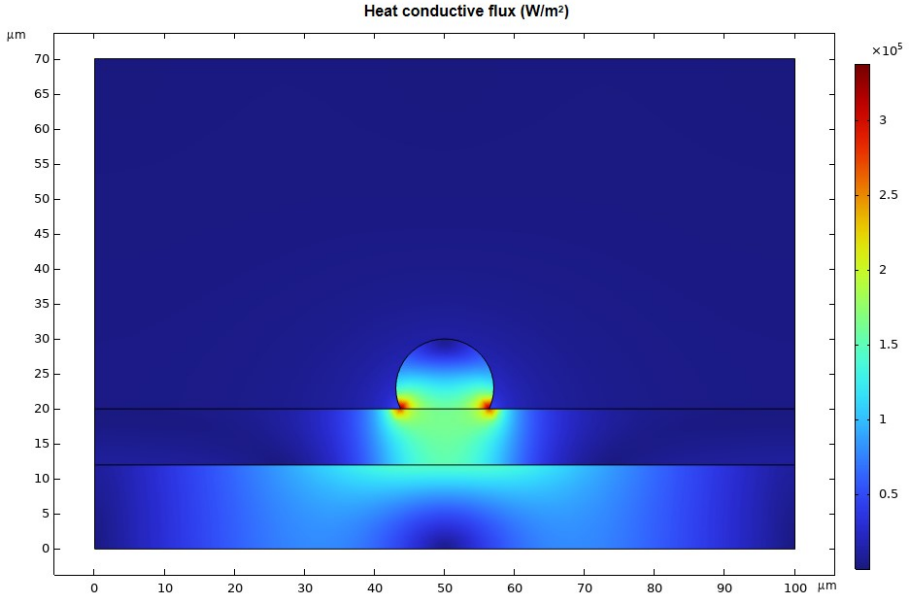

Fig. S13 The heat conduction flux of heat transfer process on the ML-SHs

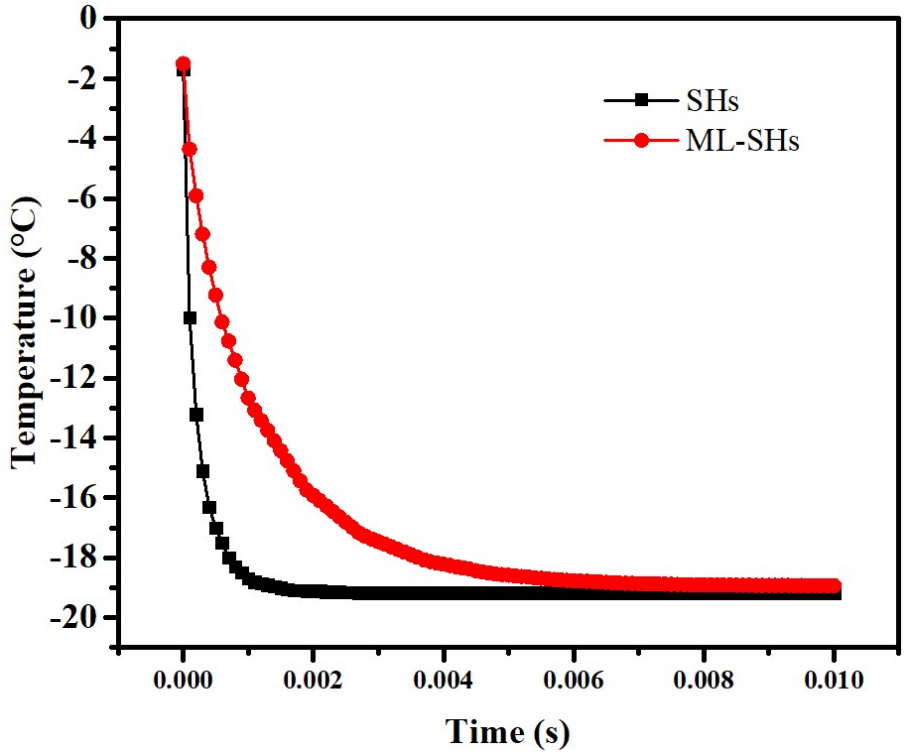

Fig. S14 The temperature changes of water droplet on the ML-SHs and SHs

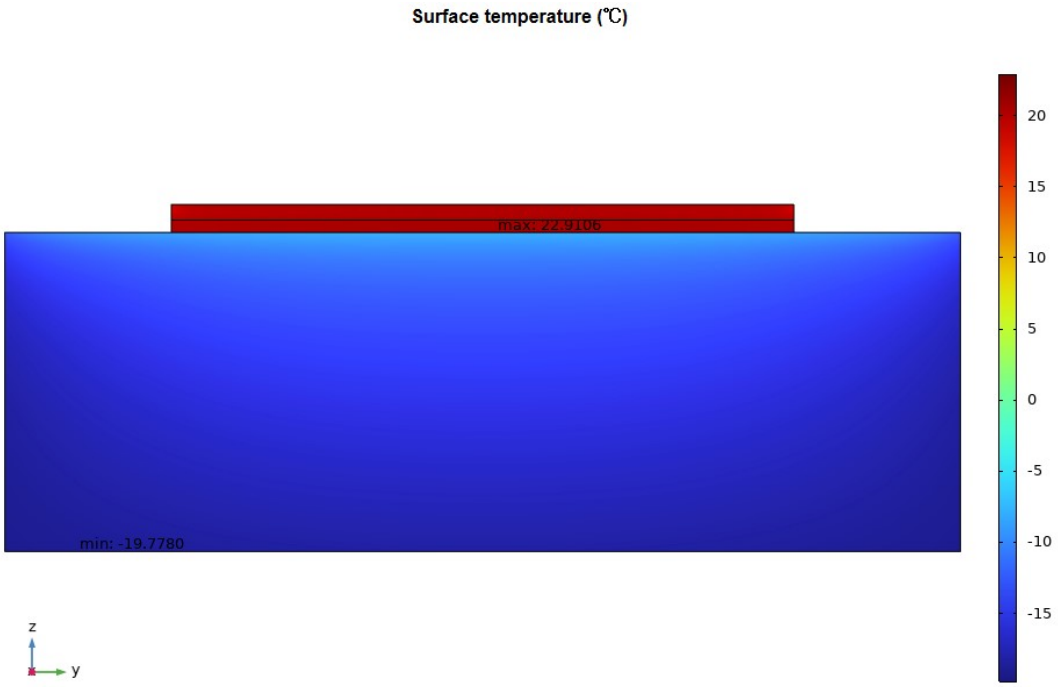

Fig. S15 The surface temperature of ML-SHs under 1 sun irradiation at -20 ℃

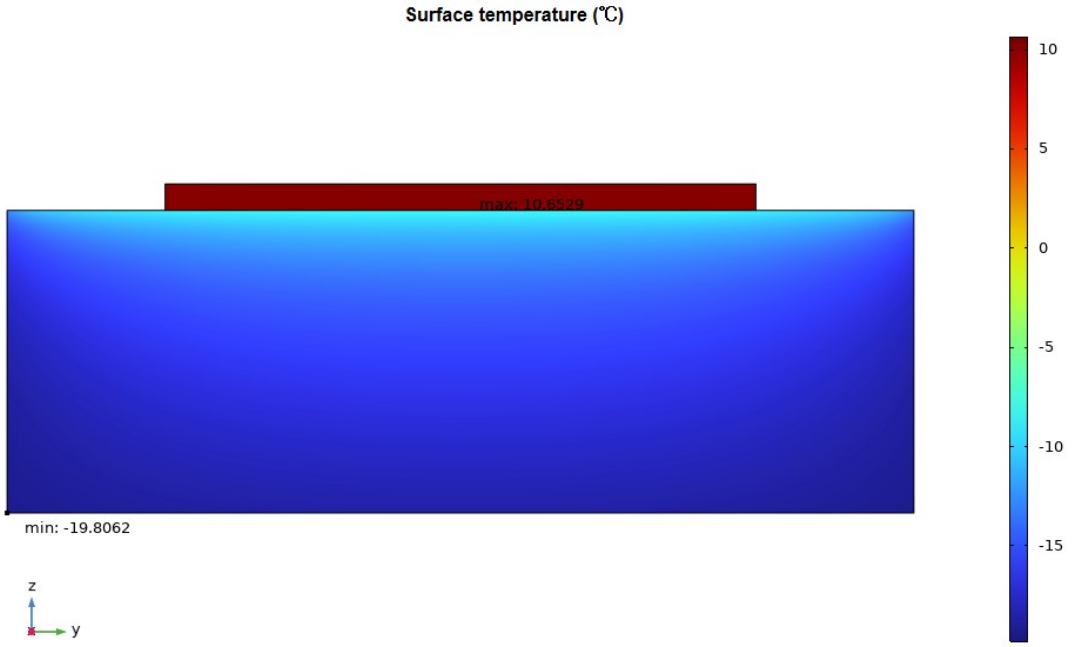

Fig. S16 The surface temperature of SHs under 1 sun irradiation at -20 ℃

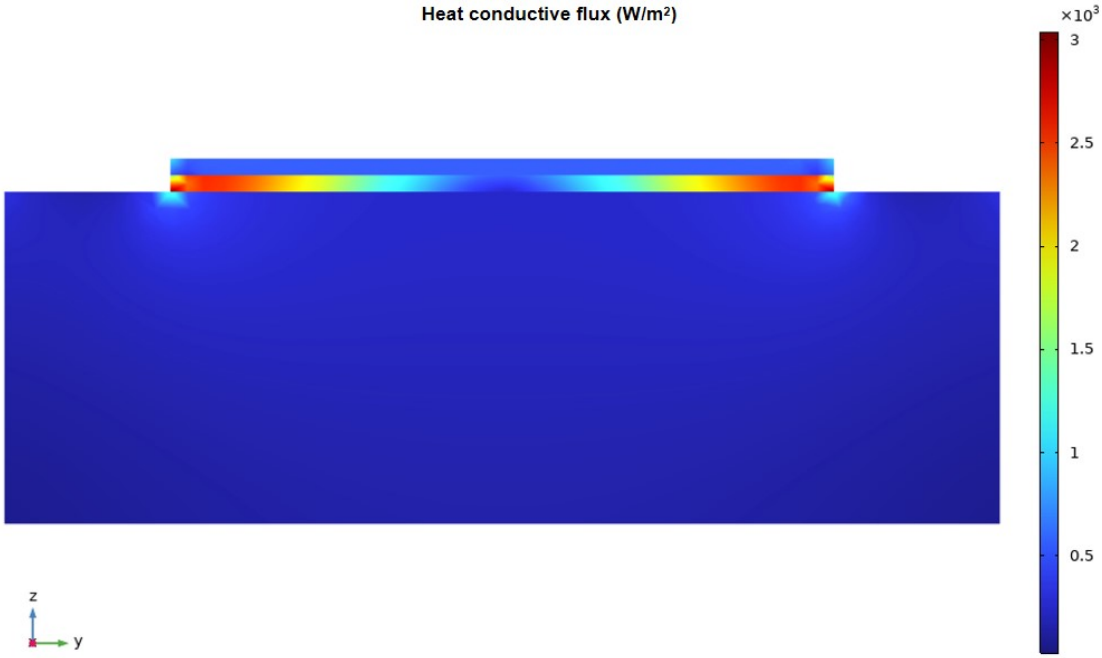

Fig. S17 The Heat conductive flux of ML-SHs under 1 sun irradiation at -20 ℃

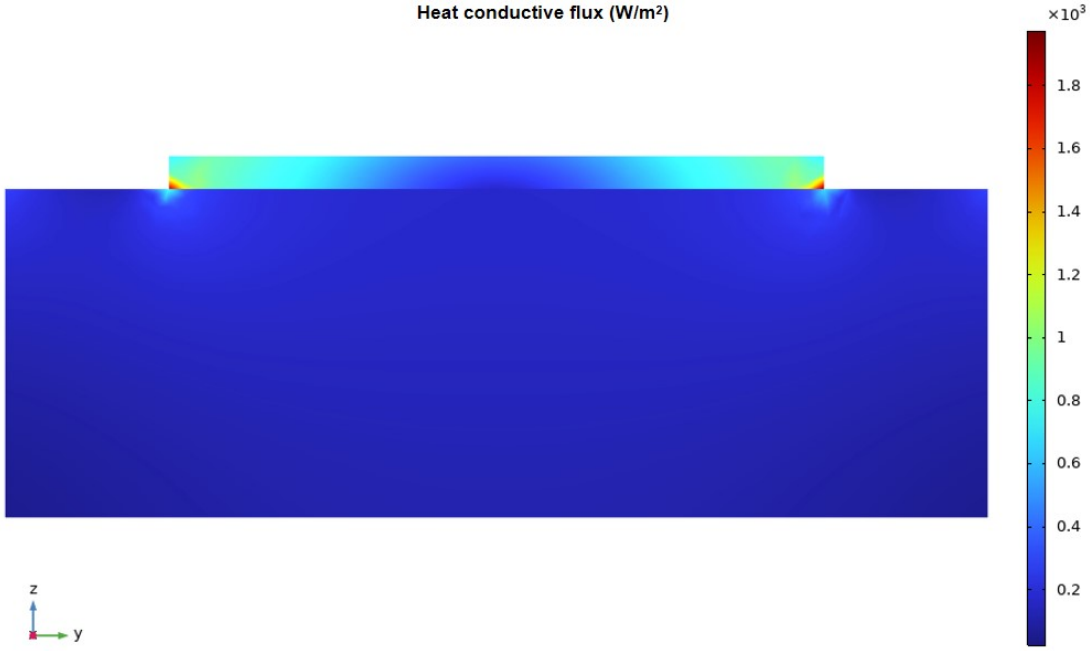

Fig. S18 The Heat conductive flux of SHs under 1 sun irradiation at -20 ℃

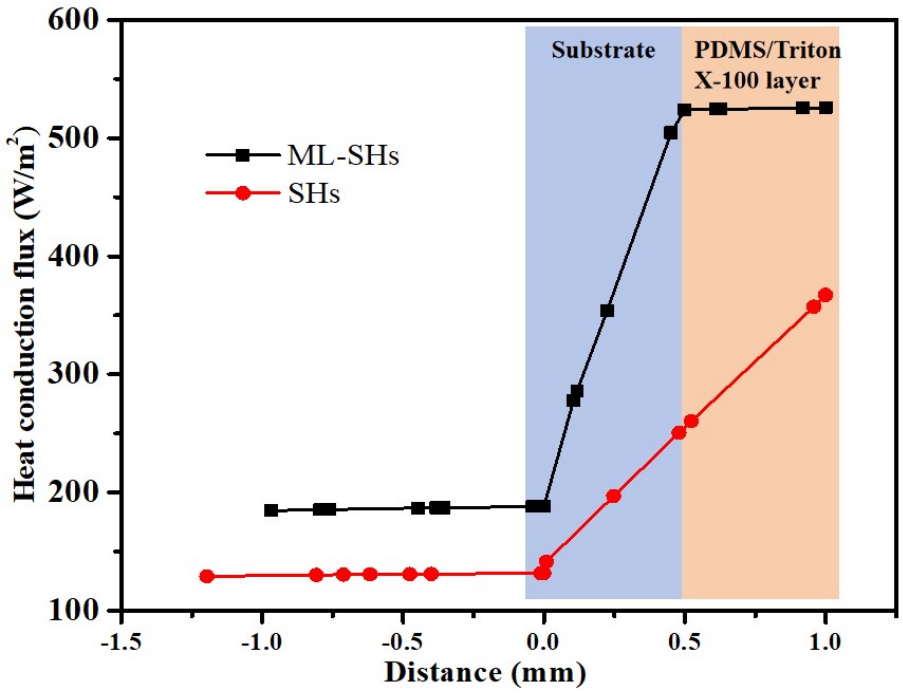

Fig. S19 The heat conduction flux distribution of samples down from top surface to the 2 mm distance surface

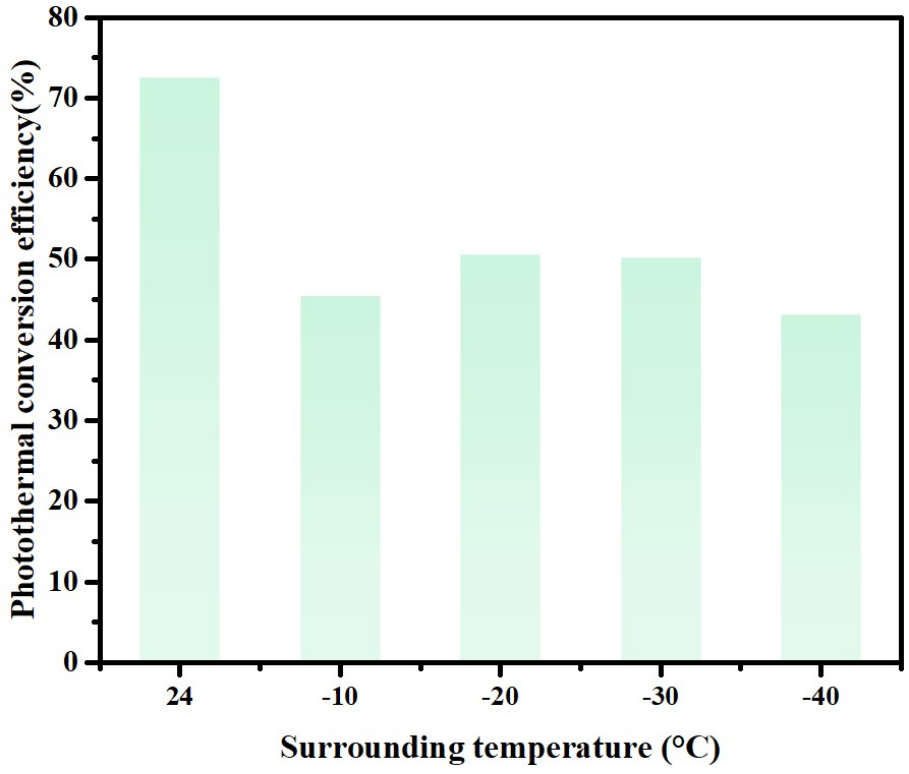

Fig. S20 The photo-thermal conversion efficiency of ML-SHs at different surrounding temperatures.

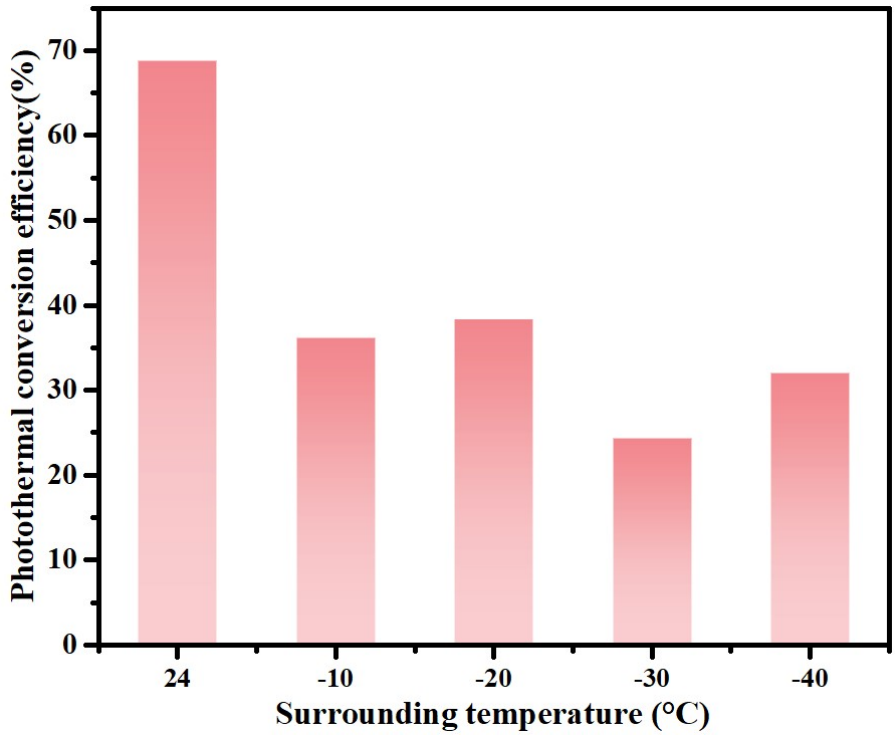

Fig. S21 The Photo-thermal conversion efficiency of SHs at different surrounding temperatures.

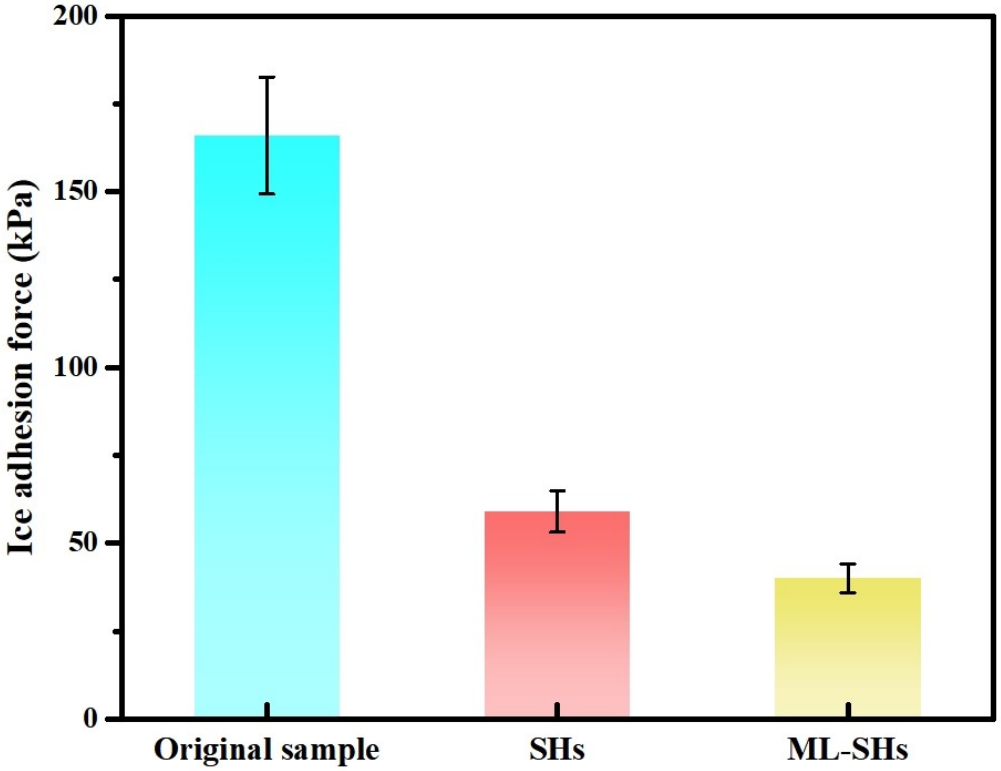

Fig. S22 The ice adhesion strength of different coatings.

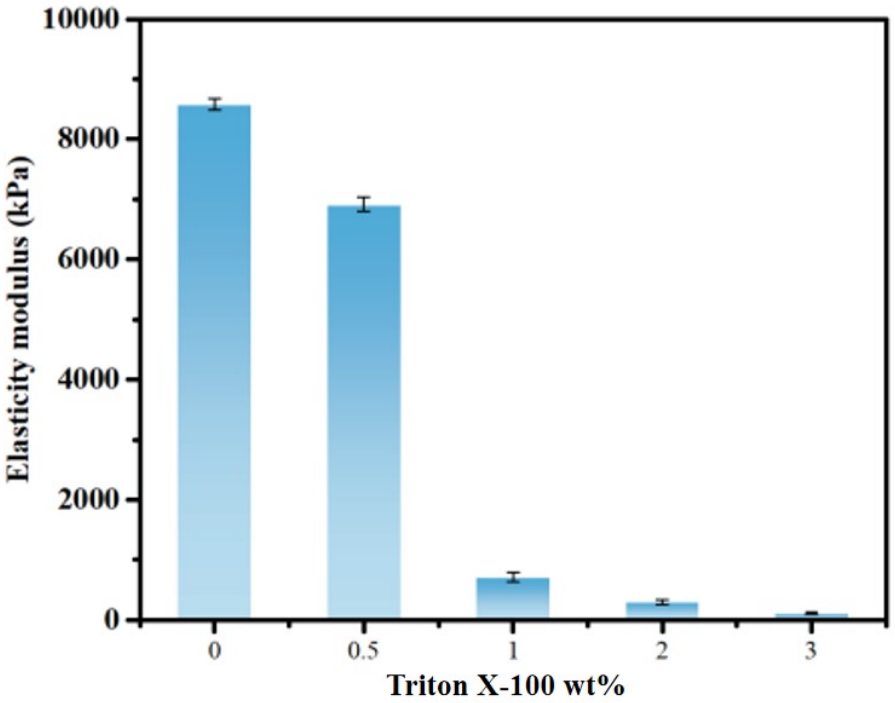

Fig. S23 The elastic modulus of PDMS/Triton X-100 layer with different addition amount of Triton X-100

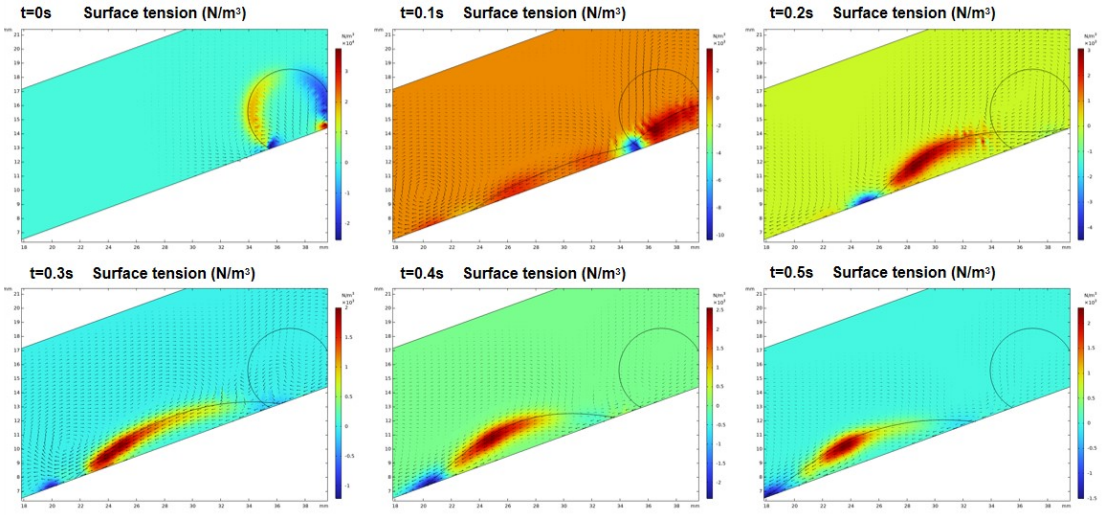

Fig. S24 Simulation of surface tension and flow state on the uncoated hydrophilic surfaces

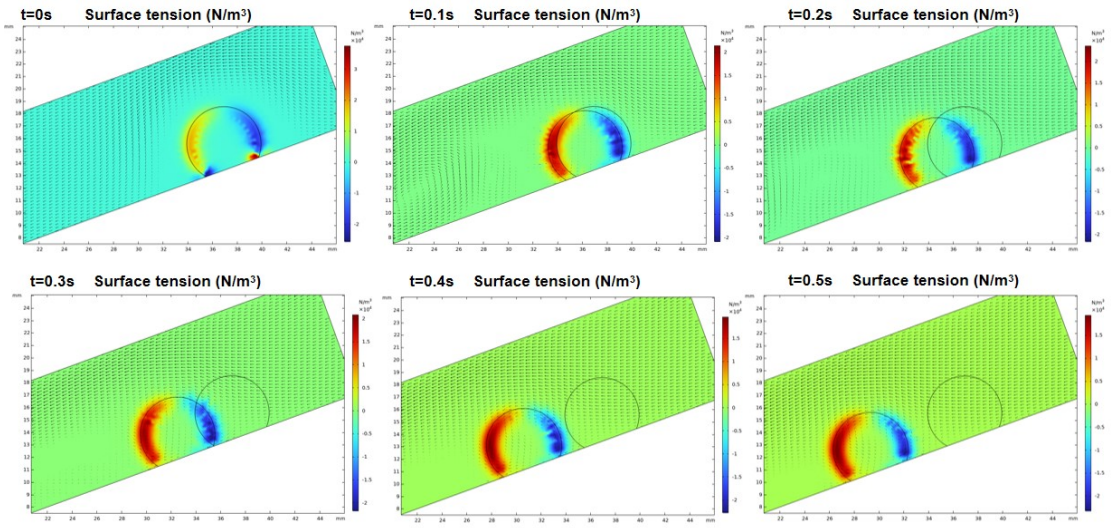

Fig. S25 Simulation of surface tension and flow state on the ML-SHs surfaces

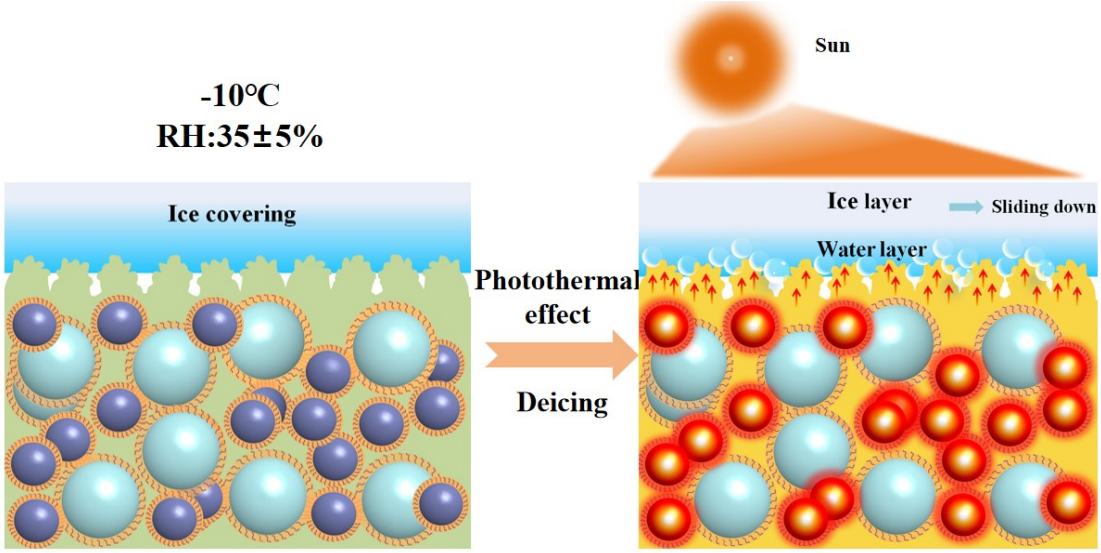

Fig. S26 Schematic diagram of the mechanism of active phtothermal de-icing

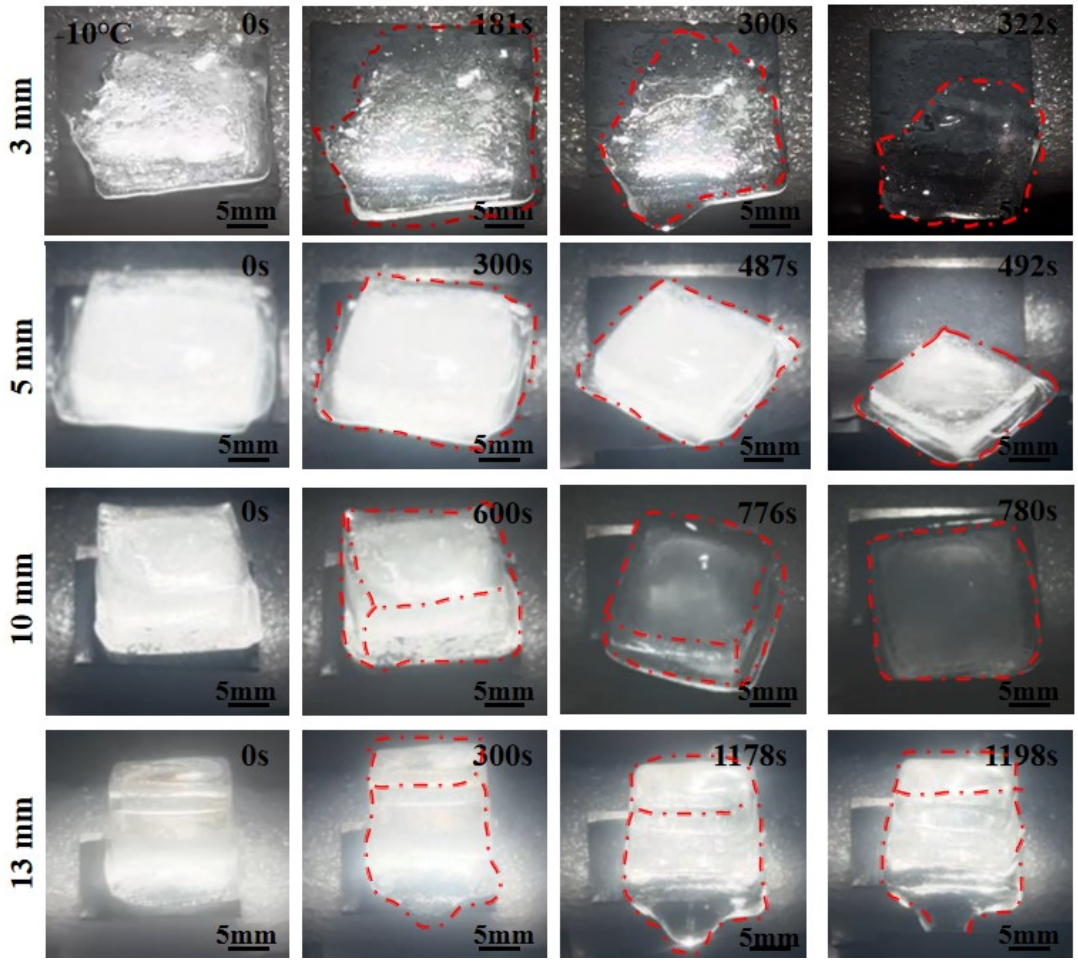

Fig. S27 Ice melting experiments with different ice thicknesses.

4. Supplementary Table

Table. S1 Comparison of ML-SHs and with previously reported literature photothermal substance content and costs

	Materials	Amount	Cost ($/m2)
[1]	TiN+SiO_2	20 wt%	6.01
[2]	TiN	0.48 g	0.67
[3]	Fe_3O_4	90 wt%	21.08
[4]	TiC	1 g	5.24
[5]	MWCNTs	0.15 g	2.01
	TiN	**0.3 g**	**0.42**
This Work	**SiO_2**	**1 g**	**0.28**
		Total	**0.7**

Table S2 Comparison of the Rate of delaying freezing time, icing melting time and surface temperature of the ML-SHs with previously reported anti-icing surfaces

Absorbs	Rate of delaying freezing time (%)	Icing melting time (s)	Tempertur e (℃)	Published year	Ref
TiN		860s (-15℃)	72	2022	[1]
TiN	113% (6μL,-15℃)	360s Drop of ice(-15℃)	15(-15℃)	2024	[2]
Fe_3O_4 NPs	4475% (5 μL, -20 ℃, RH:	480 s (-5 ℃)	7.5	2021	[3]
CB	284% (60 μL ,-20℃,RH:35±5%)	600s (-20℃)	71.9	2023	[6]
CuO	480% (10μL,-15 ℃)	405s (-15℃)	73.5	2024	[7]
GP	1500% (50μL，-10℃,RH:50±5%）	60s Drop of ice(0.5g,-10℃）	65.4	2023	[8]
TiC	540% (-15℃,RH:85±5%)	110s Drop of ice((-20℃)	64	2024	[9]
TiO_2		420s (-15℃)	32	2024	[10]

BC/TiN	1700% (10 μL, -30 ℃)	600 s (-20 ℃)	62.4	2022	[11]
Ink/nickel	2004%(10 μL, -15 ℃, RH: 25%)	723s (-10 ℃)	72	2022	[12]
TiN	**8000% (-40℃,RH:35±5%) Never freezing (-30℃)**	**817s (-30℃)**	**80.2**		**This work**

5. Supporting References

[1] Li Y , Ma W , Kwon Y S ,et al. Solar Deicing Nanocoatings Adaptive to Overhead Power Lines[J].Advanced Functional Materials, 2022, 32(25): 2113297.

[2] Ren Y, Hou M, Jiang Z, et al. Photothermal superhydrophobic composite coatings based on n-tetradecane@$CaCO_3$/TiN microcapsules for anti-/deicing[J]. Surface and Coatings Technology, 2024, 485: 130888.

[3] B. Wu, X. Cui, H. Jiang, N. Wu, C. Peng, Z. Hu, X. Liang, Y. Yan, J. Huang, D. Li, A superhydrophobic coating harvesting mechanical robustness, passive anti-icing and active de-icing performances, J. Colloid Interface Sci. 590 (2021) 301-310.

[4] J. J. Liu, C. Y. He and B. H. Liu, Z. Q. Wang, S. J. Zhao, Z. W. Lu, Y. Z. Zhang, Z. Q. Tang, X. H. Gao and X. Aday, A robust photo-thermal and electro-thermal superhydrphobic surface for all-weather anti-icing/deicing, Chem. Eng. J, 2024, 489, 151338.

[5] L. Jiang, M. Han, J. Sun, M. Gong, Y. Lin, T. Xiao, P. Xiang, W. Chen and X. Tan, Strong mechanical and durable superhydrophobic photothermal MWCNTs/SiO_2/PDMS/PVDF composite coating for anti-icing and de-icing, *Prog. Org. Coat*, 2023, 174, 107282.

[6] Zheng M, Zhou C, Liu Q, et al. Preparation and performance of anti-icing and deicing PF-POS@SiO2/CB photothermal superhydrophobic coatings for electrical insulators[J]. Soft Matter, 2023, 19(46): 9036-9049.

[7] Zhou M, Zhang L, Zhong L, et al. Robust Photothermal Icephobic Surface with Mechanical Durability of Multi‐Bioinspired Structures[J]. Advanced Materials, 2024, 36(3): 2305322.

[8] Wei X, Cai F, Wang J. Electrothermal/photothermal superhydrophobic coatings based on micro/nano graphite flakes for efficient anti-icing and de-icing[J]. Progress in Organic Coatings, 2023, 182: 107696.

[9] Liu J J, He C Y, Liu B H, et al. A robust photo-thermal and electro-thermal superhydrphobic surface for all-weather anti-icing/deicing[J]. Chemical Engineering Journal, 2024, 489: 151338.

[10] Hou M, Jiang Z, Sun W, et al. Efficient Photothermal Anti‐/Deicing Enabled by 3D Cu2‐xS Encapsulated Phase Change Materials Mixed Superhydrophobic Coatings[J]. Advanced Materials, 2024, 36(3): 2310312.

[11] Wang B, Yu P, Yang Q, et al. Upcycling of biomass waste into photothermal superhydrophobic coating for efficient anti-icing and deicing[J]. Materials Today Physics, 2022, 24: 100683.

[12] Zhang S, Zhang F, Zhang Z, et al. An electroless nickel plating fabric coated with photothermal Chinese ink for powerful passive anti-icing/icephobic and fast active deicing[J].

Chemical Engineering Journal, 2022, 450: 138328.